Biomedical Optics EXPRESS

Diabetes imaging—quantitative assessment of islets of Langerhans distribution in murine pancreas using extended-focus optical coherence microscopy

Corinne Berclaz,[1,2,*] Joan Goulley,[2] Martin Villiger,[1] Christophe Pache,[1] Arno Bouwens,[1] Erica Martin-Williams,[1] Dimitri Van de Ville,[3,4] Anthony C. Davison,[5] Anne Grapin-Botton,[2] and Theo Lasser[1]

[1]*Laboratoire d'Optique Biomédicale, École Polytechnique Fédérale de Lausanne, 1015 Lausanne, Switzerland*
[2]*Swiss Institute for Experimental Cancer Research (ISREC), École Polytechnique Fédérale de Lausanne, 1015 Lausanne, Switzerland*
[3]*Institute of Bioengineering, École Polytechnique Fédérale de Lausanne, 1015 Lausanne, Switzerland*
[4]*Department of Radiology and Medical Informatics, University of Geneva, 1211 Geneva, Switzerland*
[5]*Chair of Statistics, MATHAA, École Polytechnique Fédérale de Lausanne, 1015 Lausanne, Switzerland*
[*]*corinne.berclaz@epfl.ch*

Abstract: Diabetes is characterized by hyperglycemia that can result from the loss of pancreatic insulin secreting β-cells in the islets of Langerhans. We analyzed *ex vivo* the entire gastric and duodenal lobes of a murine pancreas using extended-focus Optical Coherence Microscopy (xfOCM). To identify and quantify the islets of Langerhans observed in xfOCM tomograms we implemented an active contour algorithm based on the level set method. We show that xfOCM reveals a three-dimensional islet distribution consistent with Optical Projection Tomography, albeit with a higher resolution that also enables the detection of the smallest islets ($\leq$ 8000 µm^3). Although this category of the smallest islets represents only a negligible volume compared to the total β-cell volume, a recent study suggests that these islets, located at the periphery, are the first to be destroyed when type I diabetes develops. Our results underline the capability of xfOCM to contribute to the understanding of the development of diabetes, especially when considering islet volume distribution instead of the total β-cell volume only.

OCIS codes: (170.0170) Medical optics and biotechnology; (170.1420) Biology; (170.4500) Optical coherence tomography; (170.6935) Tissue characterization; (100.6890) Three-dimensional image processing.

References and links

1. American Diabetes Association, "Diagnosis and classification of diabetes mellitus," Diabetes Care **34**, S62–S69 (2011).

#166531 - $15.00 USD Received 12 Apr 2012; revised 7 May 2012; accepted 10 May 2012; published 14 May 2012

2. J. A. Bluestone, K. Herold, and G. Eisenbarth, "Genetics, pathogenesis and clinical interventions in type 1 diabetes," Nature **464**, 1293–1300 (2010).
3. Y. Lin, and S. Zhongjie, "Current views on type 2 diabetes," J. Endocrinol. **204**, 1–11 (2010).
4. P. F. Antkowiak, M. H. Vandsburger, and F. H. Epstein, "Quantitative pancreatic β cell MRI using manganese-enhanced look-locker imaging and two-site water exchange analysis," Magn. Reson. Med. (Aug. 16, 2011) (e-pub ahead of print).
5. F. Souza, N. Simpson, A. Raffo, C. Saxena, A. Maffei, M. Hardy, M. Kilbourn, R. Goland, R. Leibel, J. Mann, R. Van Heertum, and P. E. Harris, "Longitudinal noninvasive PET-based β cell mass estimates in a spontaneous diabetes rat model," J. Clin. Invest. **116**, 1506–1513 (2006).
6. D. Wild, A. Wicki, R. Mansi, M. Béhé, B. Keil, P. Bernhardt, G. Christofori, P. J. Ell, and H. R. Mäcke, "Exendin-4-based radiopharmaceuticals for glucagonlike peptide-1 receptor PET/CT and SPECT/CT," J. Nucl. Med. **51**, 1059–1067 (2010).
7. M. Brom, K. Andralojć, W. J. G. Oyen, O. C. Boerman, and M. Gotthardt, "Development of radiotracers for the determination of the beta-cell mass in vivo," Curr. Pharm. Design **16**, 1561–1567 (2010).
8. L. R. Nyman, E. Ford, A. C. Powers, and D. W. Piston, "Glucose-dependent blood flow dynamics in murine pancreatic islets in vivo," Am. J. Physiol.-Endoc. M. **298**, E807–E814 (2010).
9. M. M. Martinic, and M. G. von Herrath, "Real-time imaging of the pancreas during development of diabetes," Immunol. Rev. **221**, 200–213 (2008).
10. T. Alanentalo, A. Asayesh, H. Morrison, C. E. Lorén, D. Holmberg, J. Sharpe, and U. Ahlgren, "Tomographic molecular imaging and 3D quantification within adult mouse organs," Nat. Methods **4**, 31–33 (2007).
11. T. Alanentalo, C. E. Lorén, A. Larefalk, J. Sharpe, D. Holmberg, and U. Ahlgren, "High-resolution three-dimensional imaging of islet-infiltrate interactions based on optical projection tomography assessments of the intact adult mouse pancreas," J. Biomed. Opt. **13**, 054070 (2008).
12. M. Hara, R. F. Dizon, B. S. Glick, C. S. Lee, K. H. Kaestner, D. W. Piston, and V. P. Bindokas, "Imaging pancreatic β-cells in the intact pancreas," Am. J. Physiol. Endocrinol. Metab. **290**, E1041–E1047 (2006).
13. A. F. Fercher, W. Drexler, C. K. Hitzenberger, and T. Lasser, "Optical coherence tomography - principles and applications," Rep. Prog. Phys. **66**, 239–303 (2003).
14. J. G. Fujimoto, "Optical coherence tomography for ultrahigh resolution in vivo imaging," Nat. Biotechnol. **21**, 1361–1367 (2003).
15. J. A. Izatt, M. R. Hee, G. M. Owen, E. A. Swanson, and J. G. Fujimoto, "Optical coherence microscopy in scattering media," Opt. Lett. **19**, 590–592 (1994).
16. G. J. Tearney, M. E. Brezinski, J. F. Southern, B. E. Bouma, S. A. Boppart, and J. G. Fujimoto, "Optical biopsy in human pancreatobiliary tissue using optical coherence tomography," Digest. Dis. Sci. **43**, 1193–1199 (1998).
17. P. A. Testoni, B. Mangiavillano, L. Albarello, A. Mariani, P. G. Arcidiacono, E. Masci, and C. Doglioni, "Optical coherence tomography compared with histology of the main pancreatic duct structure in normal and pathological conditions: an *ex vivo study*," Digest. Liver Dis. **38**, 688–695 (2006).
18. N. Iftimia, S. Cizginer, V. Deshpande, M. Pitman, S. Tatli, N. A. Iftimia, D. X. Hammer, M. Mujat, T. Ustun, R. D. Ferguson, and W. R. Brugge, "Differentiation of pancreatic cysts with optical coherence tomography (OCT) imaging: an ex vivo pilot study," Biomed. Opt. Express **2**, 2372–2382 (2011).
19. R. A. Leitgeb, M. Villiger, A. Bachmann, L. Steinmann, and T. Lasser, "Extended focus depth for Fourier domain optical coherence microscopy," Opt. Lett. **31**, 2450–2452 (2006).
20. M. Villiger, J. Goulley, M. Friedrich, A. Grapin-Botton, P. Meda, T. Lasser, and R. A. Leitgeb, "In vivo imaging of murine endocrine islets of Langerhans with extended-focus optical coherence microscopy," Diabetologia **52**, 1599–1607 (2009).
21. M. Villiger, J. Goulley, E. J. Martin-Williams, A. Grapin-Botton, and T. Lasser, "Towards high resolution optical imaging of beta cells in vivo," Curr. Pharm. Design **16**, 1595–1608 (2010).
22. M. S. Anderson, and J. A. Bluestone, "The NOD mouse: a model of immune dysregulation," Annu. Rev. Immunol. **23**, 447–485 (2005).
23. Y. Hori, Y. Yasuno, S. Sakai, M. Matsumoto, T. Sugawara, V. D. Madjarova, M. Yamanari, S. Makita, T. Yasui, T. Araki, M. Itoh, and T. Yatagai, "Automatic characterization and segmentation of human skin using three-dimensional optical coherence tomography," Opt. Express **14**, 1862–1877 (2006).
24. S. J. Chiu, X. T. Li, P. Nicholas, C. A. Toth, J. A. Izatt, and S. Farsiu, "Automatic segmentation of seven retinal layers in SDOCT images congruent with expert manual segmentation," Opt. Express **18**, 19413–19428 (2010).
25. I. Ghorbel, F. Rossant, I. Bloch, S. Tick, and M. Paques, "Automated segmentation of macular layers in OCT images and quantitative evaluation of performances," Pattern Recogn. **44**, 1590–1603 (2011).
26. A. Hörnblad, A. Cheddad, and U. Ahlgren, "An improved protocol for optical projection tomography imaging reveals lobular heterogeneities in pancreatic islet and β-cell mass distribution," Islets **3**, 1–5 (2011).
27. H. Nagai, "Configurational anatomy of the pancreas: its surgical relevance from ontogenetic and comparative-anatomical viewpoints," J. Hepatobiliary Pancreat, Surg, (**10**, 48–56 (2003).
28. L. D. Shultz, B. L. Lyons, L. M. Burzenski, B. Gott, X. Chen, S. Chaleff, M. Kotb, S. D. Gillies, M. King, J. Mangada, D. L. Greiner, and R. Handgretinger, "Human lymphoid and myeloid cell development in NOD/LtSz-scid IL2Rγnull mice engrafted with mobilized human hemopoietic stem cells," J. Immunol. **174**, 6477–6489 (2005).

#166531 - $15.00 USD Received 12 Apr 2012; revised 7 May 2012; accepted 10 May 2012; published 14 May 2012

29. T. F. Chan and L. A. Vese, "Active contours without edges," IEEE Trans. Image Process. **10**, 266–277 (2001).
30. S. Osher and R. P. Fedkiw, *Level Set Methods and Dynamic Implicit Surfaces* (Springer-Verlag, 2003).
31. R. T. Whitaker, "A level-set approach to 3D reconstruction from range data," Int. J. Comput. Vision **29**, 203–231 (1998).
32. S. Lankton, "Sparse Field Methods," Technical Report, Georgia Institute of Technology (July 6, 2009).
33. J. Malcolm, Y. Rathi, A. Yezzi, and A. Tannenbaum, "Fast approximate surface evolution in arbitrary dimension," Proc. SPIE **6914**, 69144C (2008).
34. A. C. Davison and D. V. Hinkley, *Bootstrap Methods and their Application* (Cambridge University Press, 1997).
35. T. Bock, K. Svenstrup, B. Pakkenberg, and K. Buschard, "Unbiased estimation of total β-cell number and mean β-cell volume in rodent pancreas," APMIS **107**, 791–799 (1999).
36. A. Clauset, C. R. Shalizi, and M. E. J. Newman, "Power-law distributions in empirical data," SIAM Rev. **51**, 661–703 (2009).
37. T. Alanentalo, A. Hörnblad, S. Mayans, A. K. Nilsson, J. Sharpe, A. Larefalk, U. Ahlgren, and D. Holmberg, "Quantification and three-dimensional imaging of the insulitis-induced destruction of β-cells in murine type 1 diabetes," Diabetes **59**, 1756–1764 (2010).
38. T. Bock, B. Pakkenberg, and K. Buschard, "Genetic background determines the size and structure of the endocrine pancreas," Diabetes **54**, 133–137 (2005).
39. E. M. Akirav, M.-T. Baquero, L. W. Opare-Addo, M. Akirav, E. Galvan, J. A. Kushner, D. L. Rimm, and K. C. Herold, "Glucose and inflammation control islet vascular density and β-cell function in NOD mice: control of islet vasculature and vascular endothelial growth factor by glucose," Diabetes **60**, 876–883 (2011).
40. P.-O. Bastien-Dionne, L. Valenti, N. Kon, W. Gu, and J. Buteau, "Glucagon-like peptide 1 inhibits the sirtuin deacetylase SirT1 to stimulate pancreatic β-cell mass expansion," Diabetes **60**, 3217–3222 (2011).
41. S. Hamada, K. Hara, T. Hamada, H. Yasuda, H. Moriyama, R. Nakayama, M. Nagata, and K. Yokono, "Upregulation of the mammalian target of rapamycin complex 1 pathway by ras homolog enriched in brain in pancreatic β-cells leads to increased β-cell mass and prevention of hyperglycemia," Diabetes **58**, 1321–1332 (2009).
42. M. Riopel, M. Krishnamurthy, J. Li, S. Liu, A. Leask, and R. Wang, "Conditional β1-integrin-deficient mice display impaired pancreatic β cell function," J. Pathol. **224**, 45–55 (2011).
43. P. L. Bollyky, J. B. Bice, I. R. Sweet, B. A. Falk, J. A. Gebe, A. E. Clark, V. H. Gersuk, A. Aderem, T. R. Hawn, and G. T. Nepom, "The toll-like receptor signaling molecule Myd88 contributes to pancreatic beta-cell homeostasis in response to injury." PloS ONE **4**, e5063 (2009).
44. D. Choi, E. P. Cai, S. A. Schroer, L. Wang, and M. Woo, "Vhl is required for normal pancreatic β cell function and the maintenance of β cell mass with age in mice," Lab. Invest. **91**, 527–538 (2011).
45. M. Chintinne, G. Stangé, B. Denys, P. In 't Veld, K. Hellemans, M. Pipeleers-Marichal, Z. Ling, and D. Pipeleers, "Contribution of postnatally formed small beta cell aggregates to functional beta cell mass in adult rat pancreas," Diabetologia **53**, 2380–2388 (2010).
46. M. Brissova, M. J. Fowler, W. E. Nicholson, A. Chu, B. Hirshberg, D. M. Harlan, and A. C. Powers, "Assessment of human pancreatic islet architecture and composition by laser scanning confocal microscopy." J. Histochem. Cytochem. **53**, 1087–1097 (2005).
47. D. Bosco, M. Armanet, P. Morel, N. Niclauss, A. Sgroi, Y. D. Muller, L. Giovannoni, and T. Berney, "Unique Arrangement of α- and β-cells in Human Islets of Langerhans," Diabetes **59**, 1202–1210 (2010).

1. Introduction

Diabetes is a major health problem that results from defective pancreatic β-cells in the islets of Langerhans, causing hyperglycemia [1]. Type I diabetes is an autoimmune disease in which T-cells infiltrate the islets, leading to the destruction of the insulin producing β-cells [2]. Type II diabetes, on the other hand, results from insulin resistance of the peripheral tissues and from insufficient compensation by β-cells [3]. According to the World Health Organisation (August 2011), 346 million people worldwide suffer from diabetes. Although many aspects of the disease mechanism are understood, several open questions about the mechanisms involved in the progression of type I and II diabetes remain. Indeed, the difficulties faced in observing individual islets in patients or live mice significantly hinder research, and limit our ability to monitor putative beneficial treatments that should protect β-cells, improve their function or promote their proliferation during diabetes.

The main challenges for imaging islets of Langerhans are (1) the localization of the pancreas deep inside the abdominal cavity, (2) the very low density of these islets in the pancreas and (3) their diverse shapes and small size, which varies approximately from 30 to 300 µm in diameter. Current non invasive clinical imaging techniques such as PET, SPECT or MRI have insufficient

#166531 - $15.00 USD Received 12 Apr 2012; revised 7 May 2012; accepted 10 May 2012; published 14 May 2012

resolution to detect individual islets and rely on a specific marker or contrast agent [4–6]. The development of a specific tracer for the β-cells is still a matter of research [7]. In order to detect individual islets optical resolution is needed. However, current *in vivo* optical techniques able to visualize β-cells *in situ* are limited in speed, penetration depth and require labeling [8–12]. Optical Coherence Tomography (OCT) [13–15] is a well-established imaging technique that provides cross-sectional views of biological tissue with micrometric resolution and has successfully been applied to a wide range of *in vivo* and *ex vivo* imaging in both clinical settings and small animal research. OCT has been applied to image fixed human pancreatic tissue [16] and the main pancreatic duct [17]. It has also been successfully employed to *ex vivo* distinguish between benign and malignant pancreatic cysts [18]. Recently, we have shown that extended-focus Optical Coherence Microscopy (xfOCM) [19] can image *in vivo* and *ex vivo* islets of Langerhans without labeling, with a spatial resolution close to cellular dimensions [20, 21]. xfOCM is based on OCT but allows to use higher numerical aperture objectives without reducing the depth of field. The increased depth of field is obtained by using an axicon in the sample arm, which generate a Bessel beam illumination. *In vivo* xfOCM pancreas imaging is possible by making a small incision through the flank of the anaesthetized mouse and by gently pulling out the duodenum encircling the pancreas. The anatomy of the pancreas allows only to access a subpart of the organ. *In vivo* xfOCM can image the surface volume of the pancreas down to 300 µm in depth. To compare xfOCM imaging of islets of Langerhans to other techniques, we dissected the pancreas of a 15-week-old NOD SCID gamma (Nonobese Diabetic Severe Combined Immunodeficiency) mouse. NOD SCID gamma mice are a well-known control for NOD mice, which spontaneously develop type I diabetes [22]. To have access to the islets of Langerhans located deeper in the pancreas, we cut the two lobes of the pancreas that are easily accessible *in vivo* into slices 250 µm thick. Segmentation and extraction of quantitative data from OCT images are challenging [23–25] but are required to facilitate and improve diagnosis. In order to obtain quantitative data, we implemented an automatic segmentation of islets of Langerhans in xfOCM tomograms based on an active contours algorithm. In this work, we performed automatic and quantitative islet imaging with xfOCM, revealing the three-dimensional size distribution of these islets. In addition, we assessed the possibility of measuring only a portion of the pancreas to extrapolate the total β-cell volume. Finally, we evaluated *in silico* the discrimination of healthy and pre-diabetic or diabetic animals based on two criteria: the total β-cell volume and the islet volume distribution.

2. Methods

2.1. xfOCM setup

The xfOCM instrument is based on a Mach-Zehnder interferometer (Fig. 1) [19]. A broadband light source (Ti:Sapphire laser, Femtolasers, Vienna, Austria; λ_c = 800 nm, $\Delta\lambda$=135 nm) is coupled into a polarization maintaining single mode fiber and then collimated and split by beam splitter BS1 into reference and illumination fields. The illumination beam passes through an axicon (175° apex angle, Del Mar Photonics) which generates a Bessel-like field with an extended focus over a length of about 400 µm. The field behind the axicon is relayed by two telescopes into the intermediate image plane (IIP), and from there demagnified by the lens combination L_t, L_s (Zeiss Neofluar, 10x, NA 0.3), resulting in a lateral definition of 1.3 µm. The illumination beam is raster scanned over the sample, typically scanning a range of 0.5 mm x 1 mm. In order to increase the field of view, the objective can also be moved by two lateral motorized scanning axes (Thorlabs, model Z812B). The light backscattered by the sample is superimposed with the reference field by beamsplitter BS2. The optical signal is analyzed through a custom spectrometer consisting of a transmission grating (1200 lines/mm) and a line-scan camera (Atmel Aviva 2048 pixels, Stemmer Imaging, Pfäffikon, Switzerland) set to an integration time of 40 µs

#166531 - $15.00 USD Received 12 Apr 2012; revised 7 May 2012; accepted 10 May 2012; published 14 May 2012

and working at an A-line rate of 20 kHz. The depth profile is reconstructed after background removal, k-mapping and Fourier analysis.

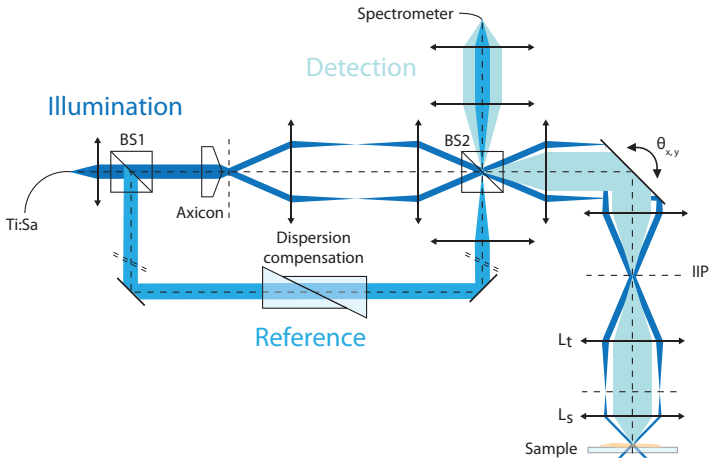

Fig. 1: Schematic layout of the xfOCM setup.

2.2. *Specimen preparation*

Anatomically, the pancreas can be segmented into three lobes [26, 27]: the splenic, gastric and duodenal lobes (Fig. 2(a)). After cervical dislocation, the duodenal and gastric lobes of a 15-week-old female NOD SCID gamma mouse (NOD.Cg-Prkdc^{scid} Il2rg^{tm1Wjl}/SzJ, Jackson Laboratory, Bar Harbor, USA) [28] were fixed for 90 min in a 10% (vol./vol.) paraformaldehyde solution in phosphate buffered saline (PBS) at room temperature, prior to an overnight incubation in a 30% (wt/vol.) sucrose solution in PBS at 4°C. The tissue was embedded in gelatin and frozen at −80°C. 34 sections of 250 µm thickness were prepared for xfOCM imaging.

2.3. *Three-dimensional image processing*

Each of the 34 sections of the gastric and duodenal lobes were imaged individually. Due to the instrument design a field of view of only 0.5 mm x 1 mm is accessible. Therefore, we performed mosaics of each slice by a lateral displacement of the objective with motorized scanning axes (Fig.2(b)). The three-dimensional imaging of the gastric and duodenal lobes resulted in more than $7 \cdot 10^8$ A-scans and represents approximately 5 Terabytes of data. The image processing was performed on the log scale, by taking $10 \cdot \log(|\mathrm{FFT}(I(k))|^2)$, where FFT is the Fast Fourier Transform and $I(k)$ is the interferogram recorded on the spectrometer. The processing time was one week on a computational cluster composed of four 8-core 2.27 GHz nodes with 48 GB of RAM and 20 Gb/s Infiniband interconnect. Figure 3 shows an example of 8 adjacent en face views of a fixed murine pancreas at different depths. The largest islet in the center extends over more than 50 µm in depth which illustrates the importance of having a 3D segmentation. In order to assess and quantify the islet shape and the ratio of islet volume to tissue volume, two segmentation tasks were performed: first, tissue versus background, defining

#166531 - $15.00 USD Received 12 Apr 2012; revised 7 May 2012; accepted 10 May 2012; published 14 May 2012

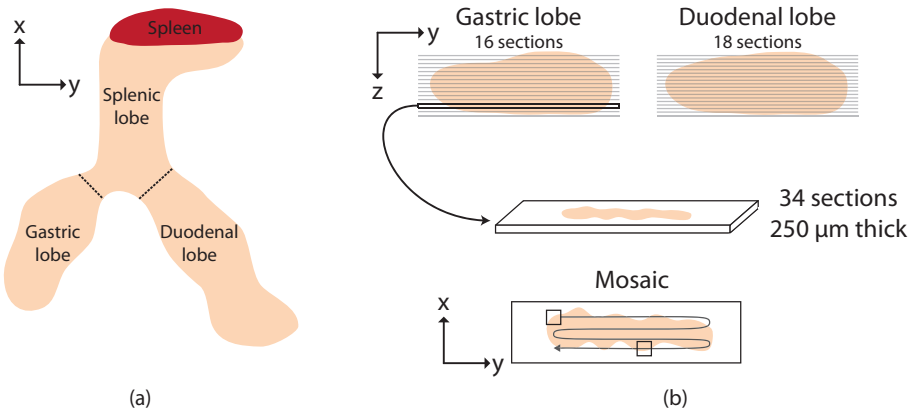

Fig. 2: (a) Schematic representation of the three lobes of a pancreas. (b) Illustration of the experimental procedure.

which fraction of the volume was filled by tissue; and, second, the islets within the detected tissue volume. The islet segmentation algorithm relies on active contours [29] with a level set method implementation [30]. The active contour model iteratively deforms an initial surface towards the boundary of the object by minimizing a function according to the properties of the image. The level set method allows tracking of the evolution of this surface using a surface of higher dimension. The initial conditions required for active contours are automatically defined from the histogram intensity of the image. The tissue segmentation relies on a cluster analysis which divides the image into two groups: tissue and background. A schematic overview of the main principles of these algorithms is illustrated in Fig. 4.

2.3.1. Segmentation of the islets of Langerhans

Definition of the initial conditions: In xfOCM tomograms, islets of Langerhans are characterized by a higher scattering signal; as a result, the islets appear as dense clouds of points of high intensity (Fig. 5(a)). One major difficulty is caused by intensity variation along the depth of the sample, caused by sample attenuation, the variation of the focal volume, and the system intrinsic sensitivity roll-off. The signal-to-noise ratio (SNR) of deep islets is reduced compared to islets near the surface. In order to obtain an automatic detection procedure, an initialization of the Active Contours algorithm (AC-algorithm) is essential. The initial conditions algorithm uses an initial adaptive thresholding step (see flowchart in Fig. 5). The adaptive threshold is fixed by using the pixel intensity distribution of each *xy*-slice. The pixel intensities appear to be roughly normally distributed, but an exponential distribution can be fitted to those above a chosen threshold intensity. We chose a higher threshold at the 0.75 percentile of this exponential distribution, allowing us to distinguish pixels belonging to islets, and also some other structures (Fig. 5(b)). Then, we applied the morphological *closing* operator to obtain filled structures (Fig. 5(c)). The Euclidean distance transform (i.e., each pixel is associated to its distance from the nearest border) of the resulting binary image is computed (Fig. 5(d)). Finally, each pixel corresponding to a regional maximum is used as the origin of a sphere of radius equal to the computed Euclidean distance of the pixel (Fig. 5(e)).

Active Contours and Sparse Field Algorithms: The AC-algorithm has several important features: (i) generation of smooth and continuous boundaries, (ii) robustness against intensity variations and speckle, and (iii) detection of objects with various shapes and sizes. The AC-

#166531 - $15.00 USD Received 12 Apr 2012; revised 7 May 2012; accepted 10 May 2012; published 14 May 2012

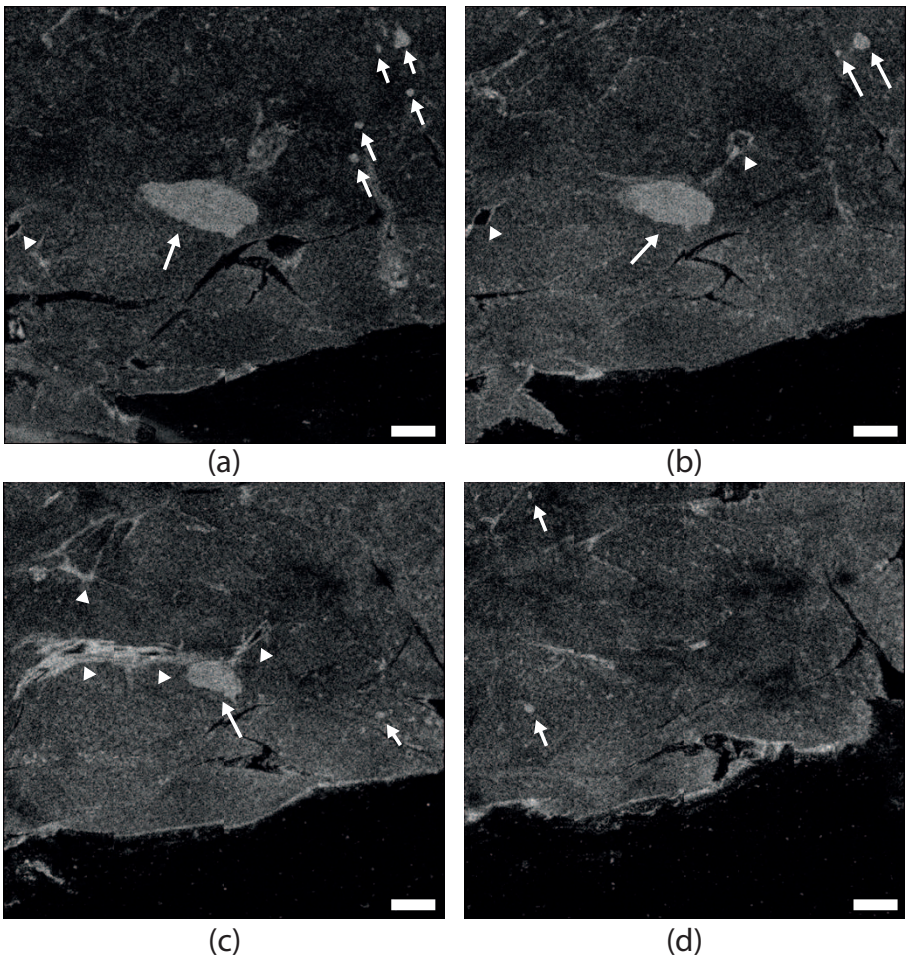

Fig. 3: Mosaic of 8 en-face views recorded on a pancreatic section. Arrows indicate islets. In addition to the islets, one can clearly observe ducts (arrowhead) and lobe structures. Each picture shows the same area but at different depth positions. (a) 11 µm in depth, (b) 54 µm, (c) 97 µm, (d) 140 µm. Scale bar: 200 µm.

#166531 - $15.00 USD Received 12 Apr 2012; revised 7 May 2012; accepted 10 May 2012; published 14 May 2012

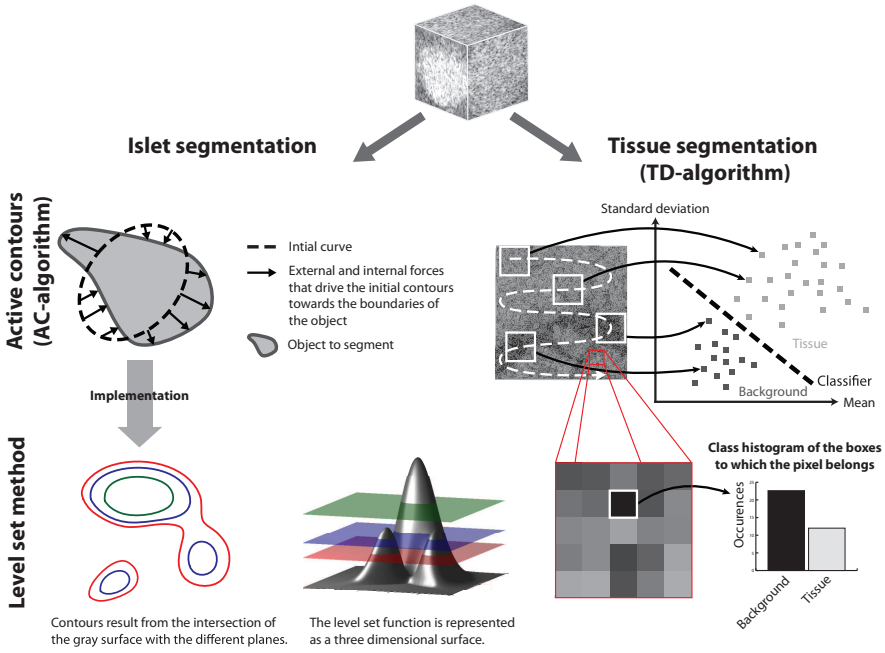

Fig. 4: Schematic 2D representation of the detection principles. The segmentation of the islet is based on an active contours algorithm starting with an initial curve which evolves towards the boundaries of the islet. The active contours algorithm is implemented with the level set method. In this example, the intersection of the grey 3D surface with the plane in blue creates a 2D contour. By moving this plane up (in green) and down (in red), one can make the contour evolve, and even split or merge. The segmentation of the tissue is based on a cluster analysis.

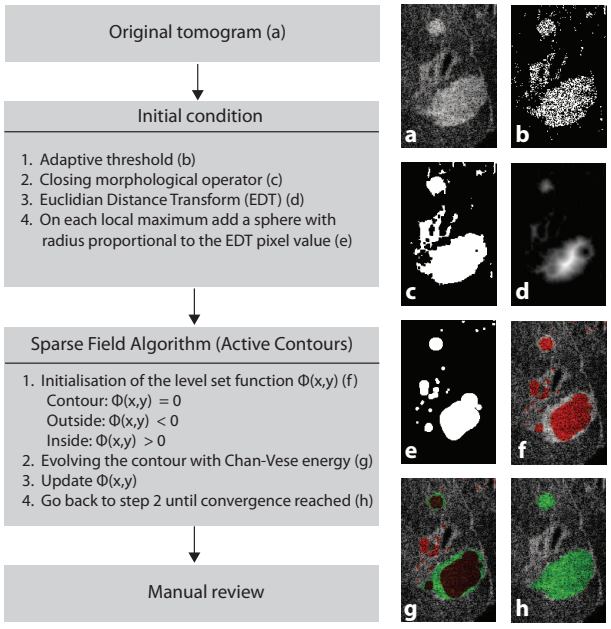

Fig. 5: Flowchart and illustration of the different steps for islet segmentation.

#166531 - $15.00 USD Received 12 Apr 2012; revised 7 May 2012; accepted 10 May 2012; published 14 May 2012

algorithm searches for the boundary of an object by using a surface that deforms under external and internal forces (Fig. 4). External forces are computed based on image properties, whereas the internal forces depend only on the curve geometry. Usually, external forces drive the curve or the surface to the edge of the object, whereas the internal force tends to keep the curve or the surface smooth. Among the numerous variations of the AC-algorithm, we used the Chan-Vese algorithm [29] which proved to be the most efficient for this type of dataset. Each image was normalized according to an adaptive threshold based on the histogram. In addition, saturated pixels or black pixels were discarded in order not to take artefacts or areas without tissue into account. One drawback of the AC-algorithm is the requirement for initial conditions. In our study, these were automatically defined based on the pixel intensity of the image, as explained above.

The evolving curve is represented using the level set method which captures *n*-dimensional surfaces as the intersection of a plane and a $(n+1)$-dimensional surface (Fig. 4). The three-dimensional surfaces are internally represented using the Sparse Field algorithm (SF-algorithm) [31], a particular efficient implementation of the level set method. Importantly, the level set method allows splitting or merging of the currently detected blobs as well as detection of several islets in parallel. In order to assess the convergence of the algorithm, we monitor the evolution of the detected volume. If the discrete derivative is less than 10^{-5} during 50 iterations, then the algorithm is stopped. The SF-code was written in Matlab and is partly based on the software package developed by J.G. Malcolm et al. [32, 33].

2.3.2. Tissue segmentation

Since one of our goal is to calculate the ratio of β-cell volume to pancreas volume, we need to compute the total volume of tissue. The general idea behind the tissue detection algorithm (TD-algorithm) presented hereafter is to classify each pixel into one of two categories: tissue or background. The TD-algorithm has two main steps (Fig. 4; Fig. 6 provides a more detailed flowchart of the algorithm). First, a large dataset of spatial features is built by scanning the whole image with overlapping boxes of fixed size. To each box we associate one two-dimensional data point $p = (\mu, \sigma)$ where μ is the mean and σ is the standard deviation of all pixels within the box, without taking into account pixels with extreme values (i.e., black or saturated pixels). Boxes with extreme mean values are removed from the dataset before performing a cluster analysis using the `kmeans` function in Matlab. Finally, we use a linear classifier to find the line that separates the two clusters found by the `kmeans` function. The second step consists in attributing to each pixel a score that depends on the boxes the pixel belongs to; i.e., the number of boxes classified as tissue minus the number of boxes classified as background. Then, based on its score, each pixel is set as tissue or background.

2.3.3. Validation

The efficiency of segmentation of the islets was determined using two criteria: the number of islets detected and the detection accuracy over a set of islets of different shapes and sizes and with various intensities. The number of islets detected by the algorithm is validated against the observations of a trained user. The detection accuracy is calculated by comparing the results with the best detection ever obtained for each islet and defined as correct by a trained user; this notion of "best detection" is subtle and subjective, as it is difficult to visually evaluate the quality of detection in three dimensions. Indeed, two detections of the same islet that are both visually accurate could differ significantly after quantification in terms of volume. In such cases and for referencing, we systematically chose the detection with the highest volume defined by a trained user as correct. By using these criteria, we obtained 90% of islets detected with a relative mean square error for the volume of the islets of 30%. The error on the volume of each

#166531 - $15.00 USD Received 12 Apr 2012; revised 7 May 2012; accepted 10 May 2012; published 14 May 2012

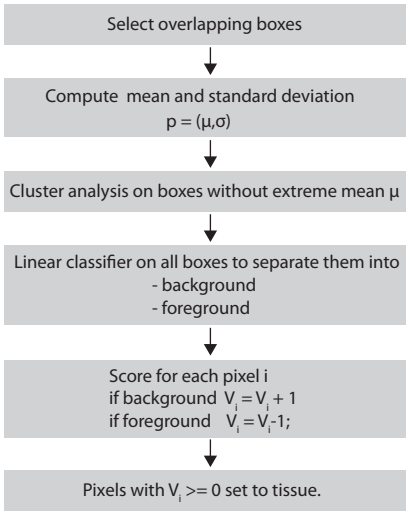

Fig. 6: Flowchart of the TD-algorithm.

islet depends on the size category, with a larger error for the small islets. A major effort was dedicated to the detection and handling of false positives, i.e., pancreas structures designated by the algorithm as islets, but rejected by a trained user (see Fig. 7). Due to the small number of islets in a pancreas, these ”false positives” have been addressed individually in order to minimize false detection. Although this step is time-consuming, it is much faster and, most importantly, much less error-prone than a manual search through thousands of tomograms. In addition, it allows the user to restart the detection with a better manual initial condition if an islet is missed or not completely detected.

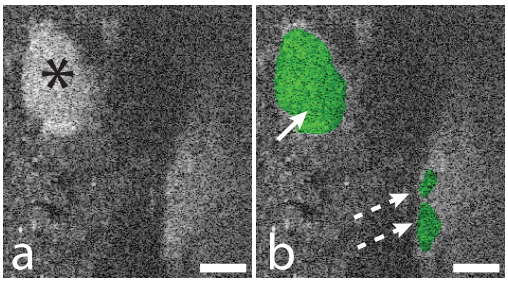

Fig. 7: The picture in (a) shows two areas with a higher intensity. By using a three dimensional view, only the area marked by a (*) is defined as an islet by a trained user. However, the result of the algorithm, shown in (b), finds three blobs. The solid arrow shows the correct detection of an islet whereas the dashed arrows indicate false positives. Scale bar: 100 μm.

3. Results

3.1. Assessing β-cell volume

The development of type I diabetes is closely related to the total β-cell volume (or calculated β-cell mass). Assessing the β-cell volume is therefore crucial to understanding and monitoring

#166531 - $15.00 USD Received 12 Apr 2012; revised 7 May 2012; accepted 10 May 2012; published 14 May 2012

diabetes onset. However, *in vivo* xfOCM can only image a subvolume of the pancreas due to its anatomy and localization into the abdominal cavity. Therefore, we asked ourselves whether we can extrapolate the total β-cell volume by imaging only a part of the pancreas. We answered this question by comparing the β-cell volume extrapolated from a part of our data with the total β-cell volume obtained from the complete *ex vivo* measurements. Following an approach called bootstrapping in statistics [34], we re-sampled the data for varying sample sizes. For each sample size, we re-constructed 2500 random samples and calculated the resulting percentage of β-cell volume per pancreas volume. Figure 8 shows the variability in the error obtained by comparing the percentage of β-cell volume per pancreas volume extrapolated from the small sample and the true value from the comprehensive experimental measurement. This procedure shows that we cannot reliably extrapolate the β-cell volume based on small samples of the pancreas. Indeed, even for 50% of the measured tissue, the relative error is still around 30%. This result outlines the difficulty in determining, at least on a mouse model, the total β-cell volume.

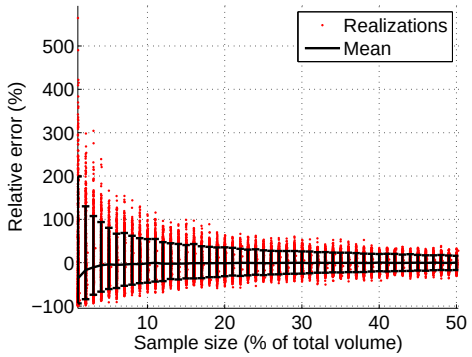

Fig. 8: Relative error for the extrapolated percentage of β-cell volume per pancreas volume based on different sample sizes. Each red circle represents the results of an individual trial. The black near-horizental line represents the median and the vertical black error bars show the 5th and 95th percentile. Even if the median relative error is below 5% for 5% of the total volume, the spreading error is still of 57% for 25% of the tissue.

3.2. 3D islet distribution in the duodenal and gastric lobes

The resolution of xfOCM offers the possibility to determine the whole islet volume distribution instead of looking at an integral value such as the total β-cell volume. According to Bock et al., the mean β-cell volume is 1280 µm^3, which corresponds roughly to 150 voxels [35]. Therefore, objects smaller than the volume of a β-cell are considered below threshold and have been automatically discarded. After a manual review of the output of the algorithm, we detected 924 islets in the duodenal and gastric lobes of a 15-week-old NOD SCID gamma mouse. A histogram with logarithmic binning shows that the smallest islets ($\leq$ 8000 µm^3) are the most common, and account for 20% of the total number of islets (Fig. 9(b)). However, this category contributes only 3% of the total β-cell volume (Fig. 9(c)), whereas the largest islets ($\geq 4\times10^6$ µm^3) contribute more than 45% of the β-cell volume and represent 4% of the total islet number. The important contribution of the small islets can, therefore, only be discovered by plotting the islet volume distribution and would be undetectable in the integral β-cell volume. The largest islet found has a volume of 9×10^6 µm^3. The total volume of β-cells corresponds to 0.26 mm^3, which yields a percentage of β-cell volume per pancreas volume of 0.175%. The

#166531 - $15.00 USD Received 12 Apr 2012; revised 7 May 2012; accepted 10 May 2012; published 14 May 2012

islet volume distribution seemed to follow a power law. We verified this hypothesis by fitting different discrete power law distributions (Yule–Simon, Zeta, Zipf and Zipf–Mandelbrot) to the islet volume data. After goodness of fit testing [36], only the Zipf–Mandelbrot distribution appears to fit the data at this level of discretisation (Fig. 9(a)):

$$f(k;N,q,s) = \frac{(k+q)^{-s}}{\sum_{i=1}^{N}(i+q)^{-s}}, \quad k = 1,\ldots,N, \tag{1}$$

with $N = 600$, and estimated parameters $q = 0.45$ and $s = 1.55$ (Fig. 9(a)).

The principle of goodness of fit testing is to compare the empirical distance (i.e., the distance between the experimental data and their fitted distribution) with an artificial distance (i.e., the distance between artificial data generated according to the hypothesized distribution and their fitted distribution). When the number of bins is large (> 500), the discrete chi-square distance becomes computationally intractable. In this case, because the number of bins is sufficiently large, we used the continuous Kolmogorov–Smirnov distance. The p-value corresponds to the proportion of trials where the artificial distance exceeds the empirical one, and in this case is 0.17, estimated from 2500 simulated artificial datasets, so we conclude that our data are close to following a Zipf–Mandelbrot law, at least at this discretization.

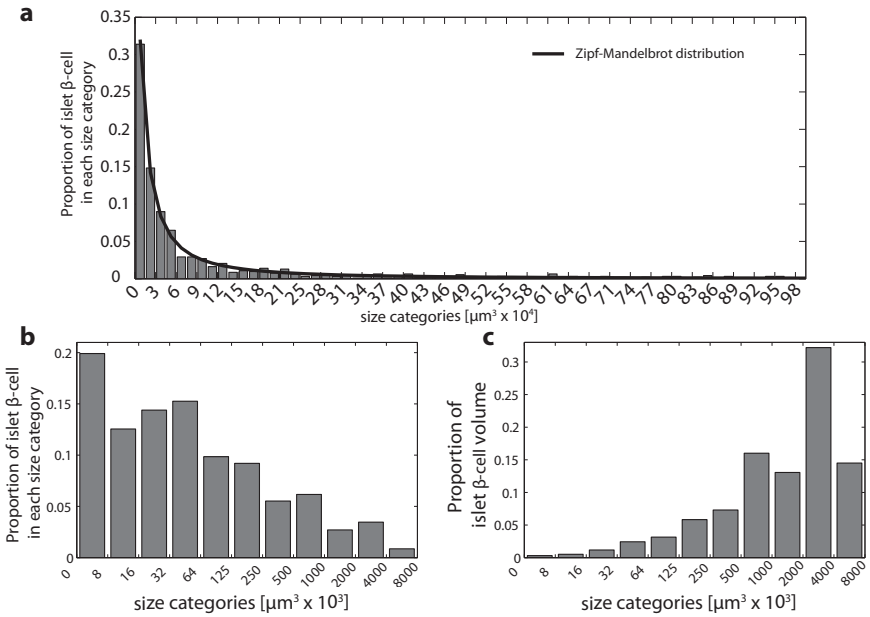

Fig. 9: Histogram of the islet volumes in the gastric and duodenal lobes of a 15-week-old female NOD SCID gamma mouse. The islet volume distribution follows a Zipf–Mandelbrot distribution (a). A logarithmic visualization of the size categories shows that the most common islets are those of volume less than 8000 µm^3, followed by those between 32000 and 64000 µm^3 (b). The proportion of the islet volume of each size category to the total β-cell volume is inversely related to their occurrences, with the smallest categories of 8000 µm^3 contributing only 3% (c).

3.3. Different distributions between the duodenal and the gastric lobe

Interestingly, we noticed that the distribution of islet volumes from the gastric lobe is different from that in the duodenal lobe: we found 315 islets in the gastric lobe and 609 islets in the duodenal lobe, even though the total β-cell volumes are comparable (0.129 mm^3 and 0.132 mm^3

#166531 - $15.00 USD Received 12 Apr 2012; revised 7 May 2012; accepted 10 May 2012; published 14 May 2012

respectively). The total tissue volumes of the gastric and the duodenal lobes were 70.79 mm^3 and 78.47 mm^3. Both islet distributions follow a Zipf–Mandelbrot law (Fig. 10). Thus the duodenal lobe contains more small islets than the gastric lobe.

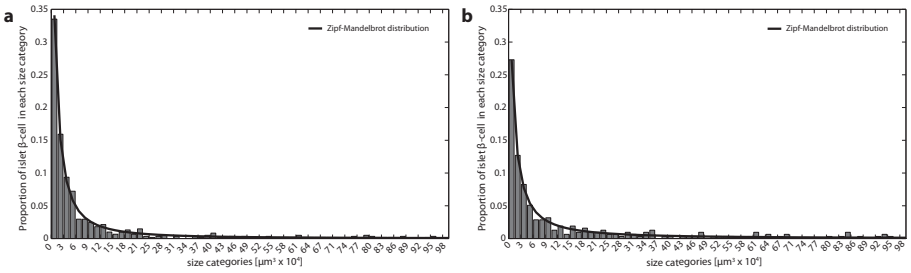

Fig. 10: (a) Histogram distribution of the duodenal lobe and (b) of the gastric lobe. The Zipf-Mandelbrot parameters are $N = 600$, $q = 0.56$ and $s = 1.65$ for the duodenal lobe and $N = 600$, $q = 0.38$ and $s = 1.41$ for the gastric lobe, with a p-value of 0.11 and 0.7, respectively.

3.4. In silico discrimination of healthy and sick animals

We cannot extrapolate the total β-cell volume of an animal by analyzing only a subvolume of the pancreas. Due to the anatomical configuration around the pancreas, only a small portion is accessible *in vivo*. Therefore, extrapolation of the total β-cell volume in a living animal is almost impossible. However, this might not preclude the possiblity to discriminate between healthy, pre-diabetic or diabetic mice (hereafter referred as *sick* mice). A full study is well beyond the scope of this project, given the variability across the different animals, which would demand a large cohort of animals. Therefore, we propose an *in silico* approach consisting of generating simulated islet datasets of a sick mouse, and detecting deviation from a healthy situation based only on a subvolume. To date, not much is known about the dynamics leading to the apoptosis of β-cells in type I diabetes. The work of Alanentalo et al. suggests that the smallest islets are the first to disappear in NOD mice and that the T-cells infiltration does not seem homogenous throughout the whole organ [37]. One may hypothesize that at first only the smallest islets disappear or all islets are attacked at the same rate, therefore leading to the earlier destruction of the smallest islets. However, the reality might involve more randomness and the islets might be attacked at different rates. Therefore, we propose for our *in silico* analysis three scenarios in an attempt to simulate this degenerative process: (A) all islets smaller than a certain size are removed from the dataset, (B) all islets are shrunk by a certain percentage in volume, and (C) a stochastic approach in which islets are attacked with a predetermined probability. The latter approach involves two parameters: (i) the probability that an islet is attacked, and (ii) the conditional probability that each individual cell is destroyed given that the islet is attacked. By applying these three scenarios to the healthy experimental data, we obtain a set of simulated datasets of sick mice. Further on we asked the question, which percentage of the tissue should be analyzed to discriminate a deviation from a healthy situation. For this approach, we can apply to these datasets the same bootstrapping method as described previously. To this end, we selected small samples of variable volume at random locations within the tissue until we obtain the desired volume. For this analysis, we can try to use either the β-cell volume or the islet volume distribution as a criterion to detect a deviation from a healthy situation. The β-cell volume would indicate an onset of the disease if it is smaller than a given threshold. Importantly, this threshold must account for the intrinsic variability of the underlying dataset. In our case, the threshold is fixed to the 0.1 percentile of the variability of the percentage of β-cell volume per pancreas volume obtained by bootstrapping in Fig. 8, thereby leading to a 10%

#166531 - $15.00 USD Received 12 Apr 2012; revised 7 May 2012; accepted 10 May 2012; published 14 May 2012

tolerance of false positives. For the islet volume distribution criterion, we compared re-sampled distributions from the sick and healthy datasets. To achieve that, we apply the Kolmogorov-Smirnov non-parametric statistical test. Figure 11 and Fig. 12 show the success rate to detect a deviation, which is indicated by the colorbar. In all scenarios, the ability to detect a deviation based on the islet volume distribution performs far better than the integral criterion based on the total β-cell volume. In scenario A, if all islets smaller than 20'000 µm^3 are destroyed, then the proportion of successful detection is 30% even for small sample sizes of 1.5% of the total measured volume. If we double this volume to 6% we can reach 60% of successful detection of diabetes onset. In scenario B, the difference between the two criteria is less pronounced; yet, the islet volume distribution performs better. The results become conclusive only for high percentages of reduction. Scenario C exhibits less favorable results, but it illustrates again the superiority of a diagnostic approach based on distributions rather than solely the total β-cell volume. However, it becomes reliable only for high probabilites of an islet being attacked and that individual β-cell are destroyed. Overall, this *in silico* study indicates an alternative way to determine diabetes onset and evolution. A distribution based criterion in contrast to the integral β-cell volume criterion seems to be a more sensitive diagnosis for the onset of type I diabetes.

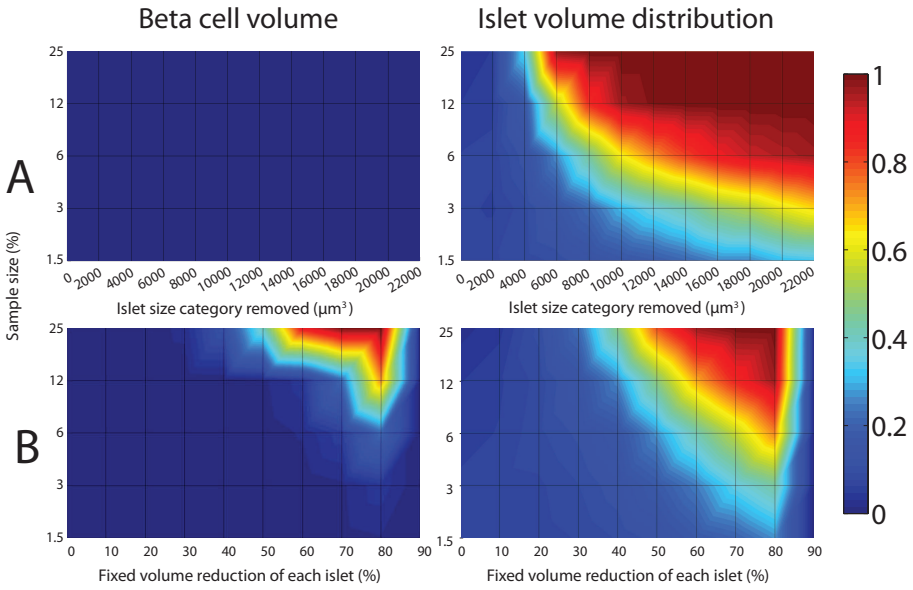

Fig. 11: Success rate to detect a deviation between the healthy and simulated sick datasets for scenarios A and B. The colorbar indicates the proportion of successful detection over 2500 trials.

4. Discussion

In this study, we described the complete three-dimensional distribution of islets of Langerhans in the duodenal and gastric lobes of a 15-week-old female NOD SCID gamma mouse. An alternative estimation of the islet distribution in a pancreas was done *ex vivo* using Optical Projection Tomography (OPT) [10]. Although we analyzed only the duodenal and gastric lobes of the pancreas with xfOCM, the islet distribution is similar to the distribution obtained with OPT for an entire pancreas. However, xfOCM is capable of resolving an islet size category of less than 8000 µm^3 ($\sim 6-10$ cells), which is not yet detectable with OPT [10]. The same authors recently suggested that the smallest and peripherally located islets are the first to be destroyed

#166531 - $15.00 USD Received 12 Apr 2012; revised 7 May 2012; accepted 10 May 2012; published 14 May 2012

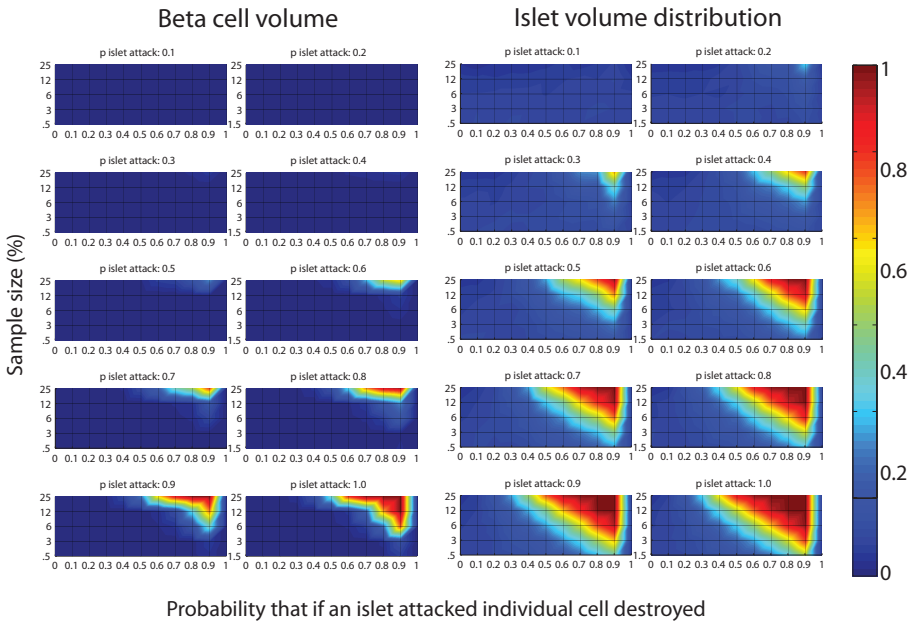

Fig. 12: Success rate for discrimination between the healthy and simulated sick datasets for scenario C. Each diagram represents a probability (p) of an islet being attacked. The x-axis shows the probabilities that if an islet is attacked the individual cell will be destroyed. The y-axis always represents the different sample size used to do the test. The colorbar indicates the proportion of successful detection over 2500 trials.

during infiltration in type I diabetes in NOD mice [37]. Therefore, even if this small size category represents only 3% of the total β-cell volume, the ability to resolve these islets might be crucial to detecting the early onset of type I diabetes. Since *in vivo* xfOCM is limited by penetration depth (300 µm) and by anatomical constraints to a small portion of the total pancreas, it would be interesting to determine the islet volume distribution in this accessible region only. However, due to the location and the morphology of the pancreas and due to the protocol of our experiment it is difficult to determine the distance of an islet to the organ's surface. A potential solution would be to image directly the entire organ in three dimensions, like in OPT. The β-cell volume per pancreas volume of 0.175% detected in our analysis is in the same range, but slightly lower than the percentages reported in the literature [38–42], although some authors report a higher β-cell volume [26, 43, 44]. It should be noted that there are significant variations between strains and across species [38]. In addition, the β-cell mass is most often given in mg and rarely with the corresponding pancreas weight or as a percentage of β-cell area per pancreas area. Finally, the majority of these imaging techniques relies on partial measurement of the pancreas and are done in two dimensions. Therefore, this lower value can be attributed to the difference between the strains and/or the use of different imaging techniques, in particular the fact that our method is three-dimensional and applied to the duodenal and gastric lobes only. Our statistical analysis reveals a huge variability on the extrapolated percentage β-cell volume which confirms the fact that the islets of Langerhans are non-homogeneously distributed throughout the pancreas [10]. This result shows that measurements based on a small part of the pancreas cannot be used to extrapolate reliably the total β-cell volume. This outcome does not confirm the statements of Chintinne et al.. They claim that 1.2% of the adult rat pan-

#166531 - $15.00 USD Received 12 Apr 2012; revised 7 May 2012; accepted 10 May 2012; published 14 May 2012

creas being systematically sampled is sufficient to obtain predictions of the β-cell mass with an error below 10% [45]. Besides the fact that the study is not based on the same species, this discrepancy might be attributed to a different experimental approach. First, they perform imaging only in two dimensions (area) whereas we have fully three-dimensional data. Second, their ground truth is the average β-cell mass measured on 2% of the pancreas of 6 rats whereas we obtain it from the complete dataset of one mouse. In this work, the experimental islet volumes follow a Zipf-Mandelbrot distribution. However, more mice would be required to conclude that a healthy islet volume distribution can be associated to a Zipf-Mandelbrot distribution. Yet, in this study we used a NOD SCID gamma mouse, which is a control for NOD mice, a reference strain for type I diabetes. Therefore we can safely assume that our islet volume distribution is indeed a reference distribution for healthy animals. Finally, the *in silico* analysis strongly suggests the superiority of islet volume distribution compared to the β-cell volume as a criterion for disease progression and detection. The islet distribution criterion performs the best in the case where small islets are removed from the dataset (scenario A in Fig. 11). The success rates become acceptable upon removal of all islets smaller than 16'000 μm^3 ($\sim$ 25 µm in diameter). However, when Analentalo et al. suggests that the small islets are the first to disappear, they are referring to islet sizes below 1'000'000 μm^3 ($\sim$ 100 µm in diameter). In our case, if we remove islets smaller than 122'000 μm^3 ($\sim$ 50 µm in diameter) we can reach a success rate of detection of 56% for only 1.5% of the total tissue imaged. In the two other scenarios (see Section 3.4), the islet volume distribution criterion still performs better than the total β-cell volume, but it is reliable only for more extreme conditions. These results underline the importance of imaging techniques that can resolve individual islets, compared to clinical imaging techniques that detect only a global signal. Although optical techniques are mainly limited to research, they provide a realm of information for a deeper understanding of type I diabetes in well-established mouse models. Nevertheless, even if diabetic mouse models are well-established, differences in the islet architecture between humans and mice should not be forgotten [46, 47].

5. Conclusion

We show that xfOCM coupled with an efficient segmentation algorithm is a label free imaging method to quantify islets of Langerhans over their whole size range ($\leq$ 8000 - 9×10^6 μm^3). Their sizes follow a Zipf-Mandelbrot distribution, which suggests a different way of monitoring diabetic type I onset. The conclusions of our statistical analysis are two-fold: first, it shows that we cannot extrapolate quantitative predictions of the total β-cell volume based on small, randomly sampled sets of measurements. Second, criterion based on the islet volume distribution shows better potential than a criterion based on the total β-cell volume alone to detect a deviation from a healthy situation. xfOCM results are consistent with the literature and have sufficient resolution to enable the visualization of the smallest islets, which is crucial for future optical diagnosis techniques of type I diabetes as well as for the development and optimization of future treatments.

Acknowledgments

This work was supported by the BetaImage Project (EU FP7-222980), funded by the European Commission within the 7th Framework Programme and by the Swiss National Science Foundation (grants 205321L_135353/1, PP00P2-123438). We thank Pascal Jermini (Information Technology Domain, École Polytechnique Fédérale de Lausanne, Switzerland) for support regarding computational resources.